Modelling Excitation Energy Transfer in Covalently Linked Molecular Dyads Containing a BODIPY Unit and a Macrocycle[†]

Cloé Azarias,[a] Lorenzo Cupellini,[b] Anouar Belhboub,[a,c] Benedetta Mennucci,[*b] and Denis Jacquemin[*a,d]

With the help of the time-dependent density functional theory coupled to an implicit solvation scheme (the polarisable continuum model), we have investigated the singlet-singlet Excitation Energy Transfer (EET) process in a panel of large BODIPY–macrocycle dyads. We have first considered different strategies to compute the electronic coupling in a representative BODIPY–zinc porphyrin assembly and, next evaluated the performances of the chosen computational protocol on several BODIPY–porphyrinoid molecular architectures for which the EET rate constants have been experimentally measured. This step showed the robustness of our approach, that is able to reproduce the magnitude of the measured rate constants in most cases. We have finally applied the validated methodology on newly designed dyads combining a BODIPY unit and an azacalixphyrin macrocycle, a recently synthesised porphyrin analogue that displays exceptional optical properties. This work allowed us to propose new molecular architectures presenting improved properties and also to highlight the interest of using the azacalixphyrin as building blocks in molecular light-harvesting antennas.

1 Introduction

Porphyrins are the most widely investigated tetrapyrrolic aromatic macrocycles due to their exceptional versatility that is illustrated by their countless applications in many research fields (chemistry, physics, material science, engineering, biology and medicine).[1] Among the specific features of these macrocycles, porphyrins display attractive optical features that are of particular interest for applications in, e.g., nonlinear optics,[2,3] ion sensing,[4,5] photodynamic therapy,[6,7] and photovoltaics.[8,9] Porphyrins typically exhibit an intense Soret absorption band at ca. 400 nm and weaker Q-bands in the 600–700 nm region. To improve their light-harvesting potential, the macrocycles can be coupled with fluorophores that present complementary absorption spectra. In this context, BODIPYs are excellent candidates. Indeed, they typically strongly absorb light at 500-600 nm, a domain in which porphyrins do not absorb. In addition, BODIPYs constitute one of the most efficient and versatile classes of fluorophores, presenting exceptional chemical stability and extremely large fluorescence quantum yields (up to 0.99).[10–13]

In this framework, molecular light-harvesting antennas coupling a porphyrin to a boron-dipyrromethene (BODIPY) fluorophore have been designed so that singlet-singlet excitation energy transfer (EET) can occur.[14–16] The BODIPY generally acts as energy donor, as it absorbs at higher energy than the porphyrins' Q-bands, and transfers it singlet state energy to the macrocycle moiety. However, the energy-level of BODIPYs can be easily tuned, and using the strongly red-shifted aza-BODIPYs, for instance, enables to obtain a reverse energy transfer, i.e., from the porphyrin to the BODIPY. As illustrated in Figure 1, several studies have characterised the EET process in molecular assem-
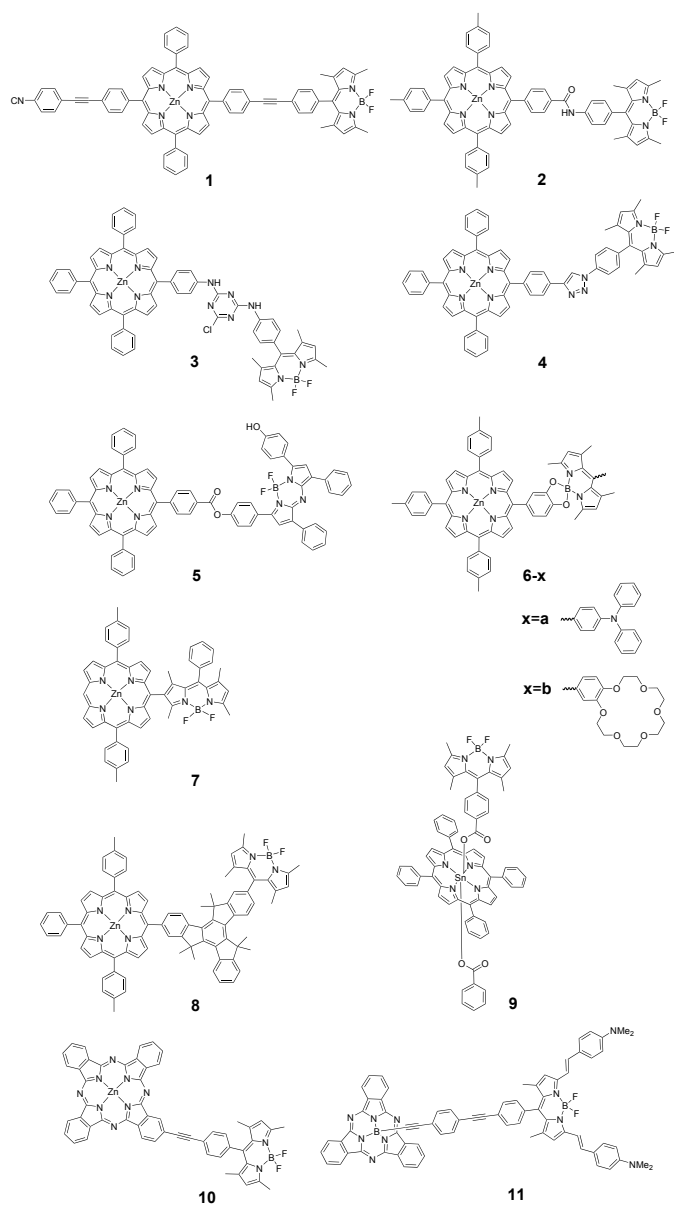
Fig. 1 Representation of the experimental dyads **1**,[17] **2**,[18] **3**,[19] **4**,[20] **5**,[21] **6-a**,[22] **6-b**,[23] **7**,[24] **8**,[25] **9**,[27] **10**[68] and **11**[56] investigated herein.

blies coupling a BODIPY with different macrocyclic systems, e.g., free-base or metalated porphyrin[17–47] phthalocyanine,[48–55] subphthalocyanine,[56–60] corrole,[61–63] chlorin,[64] chlorophyll,[65] hydroporphyrin[66] and hexaphyrin.[67]

In the present contribution, we investigate EET in BODIPY–macrocycle molecular assemblies using Time-Dependent Density Functional Theory (TD-DFT) coupled to a refined implicit solvation model, namely, the Polarisable Continuum Model (PCM) to account for environmental effects.[69] There are several methods to compute the electronic coupling starting either from the excitation calculation on the full system, e.g., using the Fragment Excitation Difference (FED) method[70] or from the separated chromophoric units, an approach that we shall name "direct coupling".[71] While the direct coupling approach computes

the electronic coupling from the transition densities of the non-interacting moieties, FED is a diabatisation scheme that recovers the electronic coupling by expressing the electronic Hamiltonian in a basis of excitation-localised states. In a first stage, we assess the methodology to compute the electronic coupling using dyad **1** (see Figure 1). Indeed, we compare the results obtained with FED and direct coupling and, for the latter, we evaluate the impact of the fragment definition, the exchange-correlation functional, and the atomic basis set, as well as the influence of the conformational freedom. Next, we estimate the accuracy of the chosen computational protocol by comparing the theoretical and experimental EET rate constants in the twelve BODIPY–porphyrinoid dyads displayed in Figure 1. Finally, we use the selected protocol to design new molecular architectures with large EET coupling between a BODIPY fluorophore and the recently synthesised aza-analogue to porphyrin, namely the azacalixphyrin (ACP).[72,73] Indeed, ACPs present remarkable optical properties with two distinct and intense absorption bands in the visible (sharp band peaking at ca. 650 nm) and near-infrared (broad band between 750 and 1000 nm) domains and they therefore stand as valuable building blocks to construct light-harvesting antennas.[72,73]

The paper is organised as follows. In the next Section, we briefly explain the methods used to model EET and the computational protocol. In Section 3, we first present a detailed study of the EET in dyad **1** (see Figure 1), comparing the coupling obtained with different strategies. Next, we compute the EET in twelve dyads for which the EET rate constants have been experimentally measured in order to assess the accuracy the chosen computational protocol. Finally, we investigate EET in ten newly designed BODIPY-azacalixphyrin dyads in order to propose new molecular dyads presenting more efficient EET processes.

2 Methods and computational strategy

In this Section, we briefly describe the two methods used to compute the electronic coupling, namely direct coupling and the Fragmentation Excitation Difference (FED) schemes and we detail our computational protocol.

2.1 Methods

In this work, we mostly assume that the electronic coupling is weak, an assumption supported by the fact that the absorption spectrum of the vast majority of the considered molecules is roughly the sum of the absorption of the constitutive chromophores, i.e., the BODIPY and the macrocycle. Within this limit, the excitation energy transfer rate can be described by the Fermi Golden rule,

$$k_{\text{EET}} = \frac{2\pi}{\hbar}|V_{DA}|^2 J, \quad (1)$$

where V_{DA} is the electronic coupling between the excited state of the donor (D) and the acceptor (A), J is the spectral overlap, i.e., the overlap integral between the normalised absorption and emission spectra of A and D ($A_A(\tilde{v})$ and $F_D(\tilde{v})$), respectively:[74–76]

$$J = \int_{-\infty}^{\infty} \frac{A_A(\tilde{v})F_D(\tilde{v})}{\tilde{v}^4} \, d\tilde{v}. \quad (2)$$

In principle, it would be possible to directly compute the lineshapes $A_A(\tilde{v})$ and $F_D(\tilde{v})$. However, a purely computational approach would require a very good accuracy on the excitation energies of both A and D, and an estimate for the broadening of the spectrum, which is generally obtained by direct comparisons with experimental spectra. The same accuracy in the spectral overlap can be obtained by directly using experimental spectra in Eq. (2), therefore we used measured spectra to determine the spectral overlap throughout this work.

2.1.1 Direct Coupling approach

Assuming a weak electronic coupling, the direct coupling approach consists in considering the D and A chromophores as separated entities. Within a first-order perturbation expansion, the electronic coupling is composed of three terms:[70,71]

$$
\begin{aligned}
V_{DA} = &\int \rho_D^{tr*}(r) \frac{1}{|r-r'|} \rho_A^{tr}(r') \, dr \, dr' \\
&+ \int \rho_D^{tr*}(r) g_{xc}(r,r') \rho_A^{tr}(r') \, dr \, dr' \\
&- \omega_0 \int \rho_D^{tr}(r) \rho_A^{tr}(r) \, dr,
\end{aligned}
\tag{3}
$$

The first term gives the Coulomb interaction (denoted as V^{coul} in the following) between transition densities (ρ^{tr}) of the donor and the acceptor, which dominates the coupling for bright transitions.[77] The second term corresponds to exchange-correlation interactions between the transition density matrices of D and A (denoted as V^{xc}),[78] g_{xc} being the exchange-correlation kernel of the selected functional. The third contribution originates in the overlap between the D and A transition densities (V^{ovlp}), ω_0 being the average resonance transition energy of the dyad. We note that within this approach, we compute the short-range coupling in addition to the Coulomb part of the coupling considered in the standard Transition Density Cube method,[79–81] which allows to assess the nature (Förster or Dexter) of the energy transfer mechanism.

In condensed phase, the interactions between the D and A moieties are screened by the surrounding environment. Within the Polarisable Continuum Model (PCM) framework, the solvent affects the coupling: (i) implicitly, through the transition properties of the fragments that are modified by the solvent polarisation; and (ii) explicitly, through an additional solvent contribution, denoted as V^{PCM}, which is given by the interaction between the transition density of the D and the solvent response to the transition of the A,

$$
V^{PCM} = \sum_k \left(\int \rho_D^{tr}(r) \frac{1}{|r-s_k|} dr \right) q(s_k; \varepsilon_\infty, \rho_A^{tr}),
\tag{4}
$$

where q is the solvent response induced by ρ_A^{tr}, and mediated by the optical dielectric permittivity, $\varepsilon_\infty = n^2$, with n the refractive index of the medium.

Therefore, the coupling used to compute the total rate constant (V^{tot}) is expressed as a sum of the above-mentioned contributions, i.e.,

$$
V^{tot} = V^{coul} + V^{xc} + V^{ovlp} + V^{PCM}.
\tag{5}
$$

In the macrocyclic molecules we considered, two quasi-degenerate excited states (denoted S_x and S_y) are involved in the electronic coupling. We thus define an effective coupling that does not depend on any rotation of these states:

$$
V^{Whole} = \sqrt{(V_{S_x}^{tot})^2 + (V_{S_y}^{tot})^2}.
\tag{6}
$$

2.1.2 Fragment Excitation Difference scheme

Fragment Excitation Difference (FED) is a diabatisation scheme based on an additional difference operator Δx, which allows to recover excitation-localised states from the eigenstates of the electronic Hamiltonian, i.e., the adiabatic states of the entire DA system. Within single-excitation methods, the matrix elements of Δx can be written on the basis of the CI amplitudes $t_{ia}^{(n)}$ and the molecular orbitals $\phi(\mathbf{r})$ by defining the *excitation density* ρ_{mn}^{ex}:[70]

$$
\rho_{mn}^{ex}(\mathbf{r}) = \sum_{ij} \sum_a t_{ia}^{(m)} t_{ja}^{(n)*} \phi_i(\mathbf{r}) \phi_j^*(\mathbf{r}) + \sum_i \sum_{ab} t_{ia}^{(m)} t_{ib}^{(n)*} \phi_a(\mathbf{r}) \phi_b^*(\mathbf{r})
\tag{7}
$$

Here, as usual, indices i,j and a,b indicate occupied and virtual MOs, respectively, and m,n refer to two excited states. It is straightforward to notice that the excitation density integrates to one if $m = n$, and to zero otherwise. Then, the excitation difference Δx_{mn} between donor and acceptor is defined as:

$$
\Delta x_{mn} = \int_{\mathbf{r} \in D} \rho_{mn}^{ex}(\mathbf{r}) d\mathbf{r} - \int_{\mathbf{r} \in A} \rho_{mn}^{ex}(\mathbf{r}) d\mathbf{r}
\tag{8}
$$

This matrix is diagonal in the basis of localised states, hence its eigenvectors define a transformation to the localised (diabatic) basis.[70,71] Its eigenvalues are 1 and -1 for D- and A-localised states respectively. The electronic Hamiltonian, which in the adiabatic basis is simply the diagonal matrix of excitation energies, can be transformed to the localised basis as well, and its off-diagonal element H_{pq} represents the electronic coupling between states p and q.

The FED method is usually detailed within a basis of two adiabatic states,[70] where Δx and H are both 2-by-2 matrices. This is valid if one assumes that the electronic eigenstates m and n are the combination of two localised states only. However, one is not guaranteed to find such states if several localised states are close in energy and mix together. Moreover, charge transfer (CT) states can mix with localised states in some cases. For the analogous fragment charge difference scheme, Yang and Hsu devised a multi-state generalisation to treat this problem, and to remove the mixing between CT and locally excited states.[82] Here we outline a similar strategy to generalise the FED method to N states.

We start by diagonalising the $N \times N$ Δx matrix, as $\mathbf{U}_1^\dagger \Delta x \mathbf{U}_1 = \Delta x'$. The diagonal matrix $\Delta x'$ contains values close, but not exactly equal, to ± 1, due to the finite eigenstate basis. By applying a threshold to the eigenvalues, we can separate the subspaces of D- and A-localised states. States with eigenvalues larger than 0.5 are assigned to the D subspace, whereas states with eigenvalues smaller than -0.5 are assigned to the A subspace. Any state with eigenvalue close to zero is removed from the calculation at this point, thus excluding CT states from the diabatisation. In each subspace, the Hamiltonian should be diagonal,[82] i.e., the

localised states should be eigenstates of the fragment Hamiltonian. To apply this additional constraint, we block-diagonalise the Hamiltonian within each subspace:

$$\mathbf{U}_2^{\dagger} \begin{pmatrix} \mathbf{H}_A & \mathbf{H}_{AD} \\ \mathbf{H}_{DA} & \mathbf{H}_D \end{pmatrix} \mathbf{U}_2 = \begin{pmatrix} \mathscr{E}_A & \tilde{\mathbf{H}}_{AD} \\ \tilde{\mathbf{H}}_{DA} & \mathscr{E}_D \end{pmatrix} \qquad (9)$$

In the final Hamiltonian, the off-diagonal block $\tilde{\mathbf{H}}_{AD}$ contains the electronic couplings between each state of D and each state of A, and $\mathscr{E}_{D/A}$ are diagonal matrices of the localised states' energies. The last transformation $\mathbf{U}_2$ is block diagonal and does not mix the D- and A- subspaces:

$$\mathbf{U}_2 = \begin{pmatrix} \mathbf{U}_A & 0 \\ 0 & \mathbf{U}_D \end{pmatrix} \qquad (10)$$

2.2 Computational details

All the calculations have been performed with a modified version of the Gaussian09 code.[83] All ground-state minima have been fully optimised using the PBE0[84] exchange-correlation functional (XCF) adding the D3 version of Grimme's dispersion approach with Becke-Johnson damping (D3[BJ])[85] in combination with the 6-31G(d) atomic basis set for all atoms but for the Sn atom that is described with the LANL2DZ effective core potential and its corresponding basis set.[86–88] For dyad **3**, we have also performed an optimisation using the D3 version of Grimme's dispersion (D3 damping).[89] Relaxed scans have been performed for dyads **1–12** by varying the dihedral angle between the BODIPY and the bridge by 30° increments. In other words, the structures considered in the rotational analysis have been re-optimised freezing the dihedral angle between the BODIPY and the bridge.

The TD-DFT transition energies, densities, and EET couplings have been computed at the PBE0[84] level of theory with the 6-31+G(d) atomic basis set except when noted. These choices of functional and atomic basis set are justified in Section 3.1.4 in which we compare the PBE0/6-31+G(d) results with others obtained with: (i) different XCF (pure generalized gradient approximation (GGA) functional, namely PBE,[90,91] the M06-L *meta*-GGA,[92] as well as the B3LYP[93] M06-2X[94] CAM-B3LYP[95] and LC-ωPBE[96] hybrids) and a reference wavefunction method, namely Equation-Of-Motion Coupled-Cluster Single and Doubles (EOM-CCSD); (ii) more extended atomic basis sets [6-311+G(d) and 6-311+G(2d,p)]. As the direct coupling calculations require to divide the molecule into fragments and hence to cut covalent bonds, we capped the free valence of each unit with one hydrogen atom as in Refs. 97 and 98. For dyads **1–12**, we have also computed the TD-DFT transition energies using the LC-ωPBE functional[96] to investigate possible charge-transfer (CT) excited states.

In order to assess the effect of mutual polarisation between the donor and the acceptor, we use polarisable QM/MM calculations (QM/MMPol), in which the excited state calculation on each fragment is performed in the presence of point charges and isotropic polarisabilities placed on the coordinates of the atoms of the other fragment.[99] The polarisability values were taken from the literature,[100] and the charges were determined by fitting the electrostatic potential consistently with the self-polarisation.[101]

Calculations of FED couplings have been performed on top of the excited state calculation of the entire molecule, that is, without cutting covalent bonds. The integrals in Eq. (8) were evaluated using Löwdin population analysis[102] of ρ^{ex}, instead of the Mulliken population used in Ref. 70. We assessed the convergence of the obtained couplings with respect to the number of excited states included in the FED diabatisation, and the robustness with respect to the definition of D and A fragments.

The solvent [chlorobenzene for **1**, o-dichlorobenzene for **2**, toluene for **3**, **5**, **6-a** and **9**, tetrahydrofuran for **4**, **8** and **10**, benzonitrile for **6-b** and **7**, dichloromethane for **11** and dimethyl-sulfoxide (DMSO) for **12–21**], effects have been introduced using the linear-response (LR) formalism[103] of the PCM approach.[69] We underline that the PCM cavity is always the same, that is, it encompasses the whole molecule, regardless of the type of calculation, optimisation or EET coupling, a statement that holds for the QM/MMPol calculation as well. The spectral overlap for known species have been determined from the measured absorption (acceptor) and emission (donor) spectra normalised on the energy scale to unit area. For determining the spectral overlap in Section 3.3, we selected the experimental emission spectrum of the BODIPY chromophore taken in Ref. 20 and shifted it on the energy scale according to the maximal emission wavelength of each tested fluorophores.

3 Results and discussion

First, we present a detailed study of the EET in dyad **1**, in order to compare the different theoretical approaches that can be used to compute the electronic coupling. Then, we estimate the accuracy of the chosen computational protocol by comparing the theoretical and experimental EET rate constants for a set of 12 BODIPY–porphyrin derivative dyads. Finally, we turn our attention toward new molecular dyads combining a BODIPY unit to an azacalixphyrin macrocycle.

3.1 Methodology to compute the EET coupling in dyad 1

In this Section, we study dyad **1** with a focus on the effects of: (i) the definition of the fragment and the role of the bridge; (ii) the chosen computational protocol in terms of exchange-correlation functional, atomic basis set, as well as the approach used to compute the couplings (direct coupling vs. FED calculations); and (iii) the relative orientation of the two moieties.

3.1.1 Fragment definition

Let us first focus on the choice of the fragment and the role of the bridge. The definition of the D and A fragments may impact the electronic excitations and hence the calculated EET rate. In Table 1, we compare the influence of the size of the fragments on the TD-DFT spectral properties as well as on the electronic coupling. We have chosen several fragments by cutting the optimised geometry of **1** at different places (see Figure S1 in the ESI[†]).

For the D part, that is, the BODIPY moiety, even though the phenyl ring at the *meso* position presents a quasi perpendicular orientation (dihedral angle of 88° between this phenyl and the core of the fluorophore), the inclusion of this ring slightly impacts the excitation energy and oscillator strength of the BOD-

Table 1 Calculated transition energies ($\Delta E^{th.}_{abs}$ in eV) and oscillator strengths (f) of the excited states of the two chromophores involved in the electronic coupling in **1** for different fragmentation schemes (see Figure S1 in the ESI†). The total coupling (V^{Whole} in cm^{-1}) is also given. The different contributions to the total couplings can be found in Table S1 in the ESI†.

| | Donor (BODIPY) | | | | Acceptor (ZnP) | | | | Coupling |
	Fragment	ES	$\Delta E^{th.}_{abs}$	f	Fragment	ES	$\Delta E^{th.}_{abs}$	f	V^{Whole}
M0	BODIPY	S_1	2.83	0.683	ZnP	S_1	2.32	0.062	2.2
						S_2	2.34	0.020	
M1	BODIPY–Ph	S_1	2.89	0.652	ZnP–Ph	S_1	2.29	0.128	3.9
						S_2	2.30	0.034	
MC1	BODIPY–Ph	S_1	2.89	0.652	ZnP–Ph–C≡C	S_1	2.28	0.159	3.4
						S_2	2.30	0.030	
MC2	BODIPY–Ph–C≡C	S_1	2.88	0.649	ZnP–Ph	S_1	2.29	0.128	3.9
						S_2	2.30	0.034	
MC3	BODIPY–Ph–C≡C–Ph	S_1	2.88	0.646	ZnP	S_1	2.32	0.062	2.4
						S_2	2.34	0.020	
MC4	BODIPY	S_1	2.83	0.683	ZnP–Ph–C≡C–Ph	S_1	2.27	0.209	3.6
						S_2	2.30	0.032	

IPY band. Indeed, when comparing **M0** and **MC4** with respect to the other fragmentation schemes, i.e., when excluding the *meso* phenyl ring from the BODIPY fragment, the transition energies (oscillator strength) are smaller by ca. 0.05-0.06 eV (larger, by ca. 0.03). Therefore, this phenyl should be included into the *D* fragment to attain reliable results. We note that a further extension of the donor fragment beyond this *meso* phenyl ring (such as in **MC2** and **MC3**) leads to trifling changes in the optical properties of the BODIPY moiety. This conclusion is consistent with our previous work focused on BODIPY dyads and triads.[98]

For the *A* fragment, that is, the zinc porphyrin (ZnP) moiety, we observe that the transition energies of the two first excited states are slightly affected by the size of the fragment (from 2.32/2.34 eV in **M0** or **MC3** to 2.27/2.30 eV in **MC4** for S_1/S_2 excited states). However, the oscillator strengths are more impacted, especially for the first excited state with an increase from 0.06 in **M0** to 0.16 and 0.21, in **MC1** and **MC4**, respectively. The fragmentation scheme **MC1** therefore stands as the best compromise to model EET in this dyad and will be used in the following of this Section. As can be seen in Table 1, the fragmentation impacts the EET couplings (the values ranging from 2.2 cm^{-1} for **M0** to 3.9 cm^{-1} for **M1**).

Finally, we performed an additional EET calculation using QM/MMpol to account for the mutual polarisation of the two fragments. Using the **M1** fragment definition, we obtained a total coupling of 3.5 cm^{-1}, only slightly lower than the **M1** coupling computed without MMPol, showing that mutual polarisation of the fragments has a marginal impact on the coupling values.

3.1.2 Excitation on the entire dyad

To corroborate the conclusions of Section 3.1.1, we studied and characterised the excited states of the full dyad. The transition energies, oscillator strengths and molecular orbital (MO) compositions of the first four transitions are listed in Table 2 and the key MOs are displayed in Figure 2. Notably, the excitation energies and oscillator strengths computed with the various fragmentation schemes (Table 1) are close to the results obtained on the entire dyad when extending the fragments, supporting the fragmenta-

tion of the dyad.

Table 2 Transition energy ($\Delta E^{th.}_{abs}$ in eV), oscillator strength (f) and molecular orbital (MO) composition of the first four excited states in **1**.

State	$\Delta E^{th.}_{abs}$	f	MO composition (CI coefficient)
S_1	2.27	0.223	HOMO→LUMO+1 (0.584)
			HOMO−1→LUMO+2 (0.383)
S_2	2.30	0.030	HOMO→LUMO+2 (0.553)
			HOMO−1→LUMO+1 (0.430)
S_3^a	2.68	0.002	HOMO→LUMO (0.696)
S_4	2.88	0.584	HOMO−2→LUMO (0.698)

^{a} Note that this state corresponds to a spurious (non-physical) charge transfer between the two units

The MOs involved in the first two quasi-degenerated states (the Q-bands of ZnP) are localised on the macrocycle moiety. Consistent with the fragmentation analysis, the HOMO and LUMO+1 orbitals are partially delocalised on the *meso* phenyl ring of the ZnP and we can also observe a very small delocalisation on the ethynyl bridge. The S_4 excited state clearly corresponds to the excitation of the BODIPY unit as the MOs involved in this electronic transition are exclusively localised on this fluorophore. Notably, a small fraction of the electronic density is localised on the perpendicular *meso* phenyl and no density appears on the bridge. This analysis therefore further supports the adequacy of the **MC1** fragmentation scheme for computing EET coupling in dyad **1**.

Notably, a low-lying CT state appears in the PBE0 calculation between the local porphyrin and BODIPY transitions. The presence of a CT state between the donor and the acceptor states could in principle influence the EET dynamics.[104] However, TD-DFT relying on standard hybrid functional with low *exact* exchange is known to yield to unphysical (spurious) CT states due to the self-interaction error.[105,106] In order to check if this CT state in dyad **1** is physical or due to the limits of the selected functional that is suited for the local states (see above), we repeated the excited state calculation using the LC-ωPBE functional, which is a long-range corrected version of PBE, and is able to provide accurate CT state energies at large electron-hole separations. The
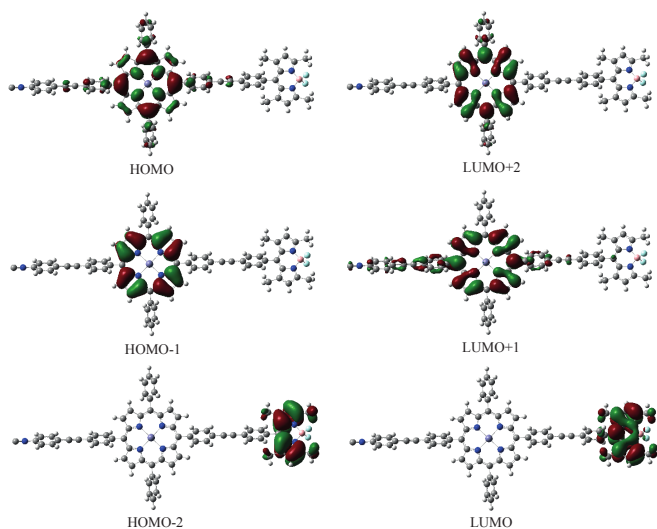
Fig. 2 Molecular orbitals (isovalue = 0.02 a.u.) involved in the first four electronic transitions of **1**.
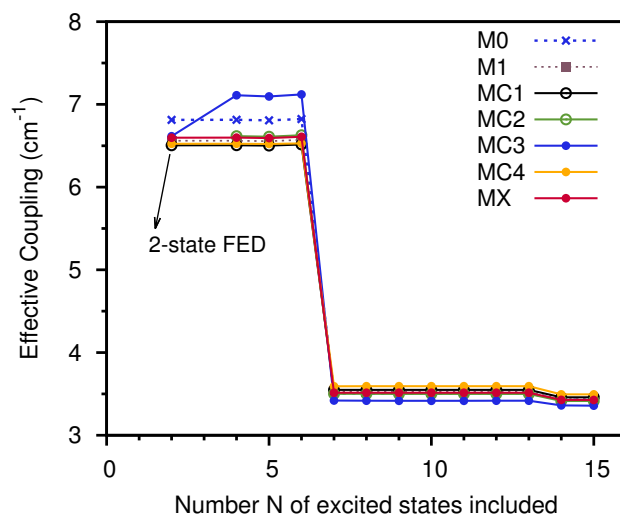

Fig. 3 Absolute total coupling (V^{Whole} in cm^{-1}) using the multi-state FED approach with different fragmentation schemes (see Figure S1 in the ESI†) as a function of the number of excited states N included in the diabatisation. The points with $N = 2$ correspond to the standard 2-state FED detailed in Ref. 70.

results are reported in Table S2 in the ESI† and no CT states are found within the first excited states with the LC-ωPBE functional, indicating that the CT state in Table 2 is spurious and should not be considered in the calculation of EET, which is what we have actually done.

3.1.3 Direct Coupling vs. FED approach

As we computed the excitation over the whole dyad, we can also compare, for the different fragmentation schemes, the results of the direct coupling approach (see Table 1) with those of the FED method displayed in Figure 3. Using the "standard" 2-state FED approach we find a coupling of ca. 6.5 cm^{-1} regardless of the fragment definition, that is, surprisingly, twice the value obtained using the direct coupling calculations (see Table 1). However, after introducing more states in the FED diabatisation (as outlined in Section 2.1.2), the coupling converges to a lower value (ca. 3.5 cm^{-1}), irrespective of the fragment definition. This value is very close to the one calculated using the direct coupling approach (3.4 cm^{-1} for the **MC1** fragmentation).

The discrepancy between the 2-state and multi-state FED approaches originates in the mixing of the BODIPY state with multiple states of the ZnP. In contrast, the 2-state FED scheme assumes that the adiabatic states are the combination of only two localised states, which is not the case in this system. The Q states are not the only states of ZnP that are mixed with the BODIPY state; in fact, when state S_7 is added to the diabatisation, the coupling drops to its final value. Notably, S_7 is localised on the ZnP and has the same orbital composition as $S_{1/2}$. In the cases where multiple donor/acceptor states are mixed in the dyad, the assumptions of the 2-state FED break down, but the multi-state FED can correctly recover the value of the electronic coupling.

As both the multi-state FED and direct coupling approaches essentially lead to the same result, we chose to adopt the latter in the following of this study. Indeed, it presents a smaller computational cost compared to FED as the calculation of the excitations of the entire dyad is not required in direct coupling calculations.

3.1.4 Influence of the atomic basis set and exchange-correlation functional

To assess the quality of description of the transition densities of both fragments, we have performed direct coupling calculations varying the underlying DFT parameters (functional and basis set) starting from the geometry optimised at the PBE0-D3$^{\text{BJ}}$/6-31G(d) level of theory.

Let us first consider the impact of the chosen exchange-correlation functional on the EET results. In Table 3, we report the transition energies and oscillator strengths of both D and A fragments, as well as the EET total coupling obtained with different exchange-correlation functionals (XCF). We notice that the coupling value is affected by the XCF, the value decreasing following the order: pure GGA > *meta*-GGA > hybrid functionals. Among the hybrid functionals, the coupling decreases when increasing the percentage of *exact* exchange included in the functional (from 3.7 cm^{-1} with B3LYP to 0.8 cm^{-1} with LC-ωPBE). In addition, we note that the oscillator strength of the first excited state of the BODIPY varies from 0.528 to 0.691 when changing the functional, and that a significant change is also observed for the porphyrin (from f=0.636/0.043 with PBE to f=0.029/0.006 with LC-ωPBE for the S_1/S_2 excited states).

This outcome hints that the XCF should be carefully chosen to obtain reliable results. Concerning the ZnP, it is well-recognised that PBE0 is well suited to model the excited state properties, as several studies successfully applied this functional to describe the spectroscopic properties of various porphyrin derivatives.[107–110] However, for the BODIPY unit, it is crucial to assess if the transition density is sufficiently well described with the PBE0 functional, as it is known that BODIPY's optical properties are not always well modelled with TD-DFT.[111] We have therefore performed an additional EET calculation considering the coupling between the transition densities of the porphyrin moiety obtained

Table 3 Calculated transition energies ($\Delta E_{abs}^{th.}$ in eV) and oscillator strengths (f) of the excited states of the donor and acceptor fragments (using the **MC1** definition, see Figure S1 in the ESI[†]) involved in the electronic coupling in **1** for different functionals. In parenthesis, the percentage of *exact* exchange (X) is given. The total coupling (V^{Whole} in cm^{-1}) is listed in the rightmost column. The different contributions to the coupling can be found in Table S4 in the ESI[†].

Method	BODIPY		ZnP		Coupling
	$\Delta E_{abs}^{th.}$	f	$\Delta E_{abs}^{th.}$	f	V^{Whole}
PBE ($X=0$ %)	2.82	0.528	2.01	0.636	4.8
			2.11	0.043	
M06-L ($X=0$ %)	2.94	0.639	2.13	0.311	4.4
			2.19	0.038	
B3LYP ($X=20$ %)	2.86	0.635	2.24	0.179	3.7
			2.26	0.032	
PBE0 ($X=25$ %)	2.89	0.652	2.28	0.159	3.4
			2.30	0.030	
M06-2X ($X=54$ %)	2.83	0.665	2.31	0.081	1.6
			2.32	0.017	
CAM-B3LYP ($X=19$–65 %)	2.84	0.678	2.23	0.067	1.2
			2.24	0.014	
LC-ωPBE ($X=0$–100 %)	2.79	0.691	2.03	0.029	0.8
			2.03	0.006	
EOM-CCSD (BODIPY) - PBE0 (ZnP)	2.84	0.561	2.28	0.159	3.1
			2.30	0.030	

with the PBE0 functional and the transition density of the BODIPY part determined at the EOM-CCSD level. Indeed, using this wavefunction method for the BODIPY part enables to avoid any XCF-dependency as well as to account for the impact of double excitations that may be non-negligible in these fluorophores.[111] The total coupling obtained with this mixed approach (bottom of Table 3) is 3.1 cm^{-1}, very close to the 3.4 cm^{-1} value determined using PBE0 for all fragments. As the computational cost of EOM-CCSD is considerably larger than that of TD-DFT, we systematically compute the EET coupling using the PBE0 functional in the following.

Let us now consider the effect of the atomic basis set. In Table 4, we report the excitation energies and oscillator strengths of both the D and A fragments and the total EET coupling computed with different bases. Only limited variations of these parameters are observed when extending the basis set to 6-311+G(d) or 6-311+G(2d,p) which therefore validates the use of the more compact 6-31+G(d) atomic basis set.

Table 4 Calculated PBE0 transition energies ($\Delta E_{abs}^{th.}$ in eV) and oscillator strengths (f) of the excited states of the donor and acceptor fragments (using the **MC1** definition, see Figure S1 in the ESI[†]) involved in the electronic coupling in **1** for different atomic basis sets. The total coupling (V^{Whole} in cm^{-1}) is also given. The different contributions to the coupling can be found in Table S4 in the ESI[†].

| Atomic basis Set	BODIPY		ZnP		Coupling
	$\Delta E_{abs}^{th.}$	f	$\Delta E_{abs}^{th.}$	f	V^{Whole}
6-31+G(d)	2.89	0.652	0.28	0.159	3.4
			2.30	0.030	
6-311+G(d)	2.87	0.655	2.27	0.147	3.1
			2.29	0.026	
6-311+G(2d,p)	2.86	0.654	2.26	0.143	3.0
			2.28	0.024	

3.1.5 Rotational analysis

Up to now, we computed the coupling considering the optimal geometry only. The experiments are generally performed at 298 K, and the relative orientation of the different units of the molecule can potentially change. We have therefore assessed the impact of the rotation on the coupling. In this framework, starting with the optimised structure of **1**, we increased, by increments of 30°, the Ψ angle, that corresponds to the dihedral angle between the two *meso* phenyl linked by the ethynyl bridge (see Figure S2 in the ESI[†]). In Figure 4, we show the evolution of the total electronic coupling and of the angle between the planes of the two A and D moieties, Φ (see Figure S2), upon rotation of angle Ψ. The values of the angles and the total couplings as well as the relative energies of the rotamers can be found in Table S5 in the ESI.[†] Unsurprisingly, the maximum (minimum) coupling value is obtained when the planes containing the core of the ZnP and BODIPY are almost collinear (perpendicular), i.e., when Φ is close to 0° (90°). We note that all rotamers present a coupling value between 1.8 and 3.8 cm^{-1} except for the unfavourable perpendicular orientation ($\Phi=82°$) for which V^{Whole} is as small as 0.8 cm^{-1}. Based on the electronic energy, the rotational barrier is ca. 1 kcal/mol, indicating a free rotation of the units around the bridge at room temperature. The average total coupling, that accounts for the total coupling of each rotamers weighted by their Boltzmann population coefficient, is 2.9 cm^{-1}, a value that is close to the total coupling obtained for the fully-optimised compound. In the following, the impact of rotational averaging is considered for several systems (*vide infra*).

We have also performed EET calculations considering different orientations for the *meso* phenyl rings of the ZnP moiety and no impact on the EET coupling could be evidenced (see Section S5 in the ESI[†]).

3.2 Comparison with experimental EET rates in dyads 1–11

In this Section, we compare the theoretical and experimental EET rate constant for a set of 12 BODIPY–porphyrin derivative dyads displayed in Figure 1. This set contains 10 BODIPY–porphyrin dyads, namely **1–9** as well as two other dyads in which the BODIPY is linked to a phthalocyanine (**10**) or a subphthalocyanine (**11**) macrocycle. We note that for all these dyads, we computed
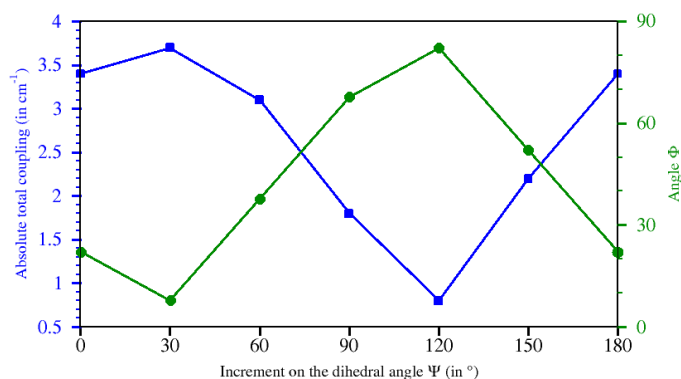
Fig. 4 Variation of the electronic coupling (V^{Whole} in cm^{-1}, blue line) and of the angle Φ (angle between the plane of the BODIPY and the ZnP moieties) as a function of the increment on the dihedral angle (Ψ) in **1**. The angles are given in degrees and are represented in Figure S2 in the ESI†. The different contributions to the coupling are listed in Table S5 in the ESI†.

the excitations using both the PBE0 and LC-ωPBE functionals (see Table S2 in the ESI†) and, similarly to the observation made for dyad **1**, all the spurious CT states between the first excited states of the BODIPY and macrocycle disappear when using the long-range corrected functional. Two borderline cases are nevertheless found for dyads **6-a** and **7** for which some LUMOs are delocalised on both the porphyrin and the BODIPY part of the molecule: there is no CT but a more coupled situation.

To compute the electronic couplings and rate constants using the "direct coupling" approach, we defined the D and A fragments according to the observations in Section 3.1, i.e., when possible, the BODIPY fragment contains its *meso* phenyl ring whereas the bridge is included in the fragment of the porphyrin moiety (see Figure S4 in the ESI†). The interested reader can find comparisons of the EET data calculated with different fragmentation schemes for each dyad in the ESI†. For all dyads, we have not only computed the EET on the fully-optimised structures but we have also accounted for the impact of rotational freedom. For each structures, we optimised several rotamers, freezing the dihedral angle between the bridge and the BODIPY unit (these angles are displayed in Figure S4 in the ESI†). In Table 5 , we report the excitation energies and oscillator strengths of both fragments as well as the total coupling and EET rate constant computed either on the fully-optimised structure or obtained from a Boltzmann averaging over the considered rotamers. We note that when several dihedral angles have been considered, we only show the results for the rotation presenting the smallest energetic barrier. Looking at the impact of the rotation, one notices that the same order of magnitude is obtained between the rate computed on the optimised geometry or from the rotational averaging except for dyads **4**, **9** and **10**. For these dyads, the larger value for the rotationally-averaged EET rate originates from the fact that the fully-optimised structures ($\Phi=0°$) do not present the "ideal" orientation between the two units and that the rotational barrier is small (below 2.6 kcal/mol). In the following, we discuss the Boltzmann EET results only, except when noted.

For 8 dyads, namely **2**, **4**, **5**, **6-b**, **8**, **9**, **10** and **11**, theory provides EET rate constants that are in good agreement with the measurements with a linear correlation coefficient R of **0.772** (the result for dyad **11** has been excluded because Ref. 56 provides a lower limit to the rate constant only). We underline that in **5** and **11**, the energy transfer occurs from the macrocycle to the BODIPY moiety, a EET direction in agreement with our calculations, as the first excited state of the BODIPY unit is calculated below the Q-bands of the porphyrinoid moieties.

Let us now discuss the cases in which the calculated EET rate constants do not seem to fit their experimental counterparts. For dyad **1**, theory underestimates the EET rate constant by one order of magnitude. Such underestimation is unexpected, given that the calculated coupling value is very robust with respect to the method used. As seen in Section 3.1, the FED scheme gives virtually the same coupling as the direct approach, which points to negligible through-bond effects. Furthermore, a high-level description of the BODIPY transition does not change the picture, therefore DFT can be excluded as a source of (major) error in our description. If, on the other hand, the DFT functional had a systematic error in the porphyrin moiety, we would underestimate also every other coupling in dyads involving a porphyrin. As a matter of fact, the Fermi Golden Rule in Eq. (1) assumes that the coupling does not depend on nuclear coordinates. However, we showed in Figure 4 that the coupling depends on bridge coordinates. If coupling fluctuations are larger than the coupling at equilibrium, the Condon approximation breaks, and Eq. (1) is not valid anymore.[112] Even though dyad **10** contains the same bridge as dyad **1**, the coupling in **10** is much larger, so that the same coupling fluctuations would be unimportant in determining the rate.

For dyad **3**, as proposed in the experimental paper,[19] we modelled the two extreme configurations: a "linear" conformation, **3l**, and a folded one, **3f**, displayed in Figures 5a and 5b, respectively. Comparing the electronic energies of both conformers with the PBE0-D3$^{\mathrm{BJ}}$/6-31G(d) scheme, it appears that the folded structure, **3f**, is more stable (by 10 kcal.mol^{-1}). Unsurprisingly, the EET rate constant computed for the least stable **3l** conformer is not fitting experiment (theory underestimates the rate by one order of magnitude). However, in the most stable **3f** conformer, the computed EET rate constant is overestimated by one order of magnitude compared to the measurements. As one sees in Figure 5b, the two moieties are extremely close and we have therefore chosen to estimate the role of the geometry on the coupling using a different empirical dispersion model to optimise the structure, namely the D3 model (the structure is displayed in Figure 5c). We used the same starting geometry as the one used for the optimisation with PBE0-D3$^{\mathrm{BJ}}$. Depending on the dispersion correction, D3 or D3$^{\mathrm{BJ}}$, we obtain a quite different distance between the two chromophores, that is, 5.3 Å versus 8.7 Å separation between the Zn atom of the porphyrin and the central *meso* carbon of the BODIPY when using the D3 and D3$^{\mathrm{BJ}}$ model, respectively. This structural modification is reflected on the coupling, that has been computed on the optimised structure, which is more than tripled when **3f** is optimized with the D3 dispersion correction instead of D3$^{\mathrm{BJ}}$ (V^{Whole}=80.1 cm^{-1}). The EET rate constant is thus one

Table 5 Calculated transition energies ($\Delta E_{abs}^{th.}$ in eV) and oscillator strengths (f) of the excited states of the BODIPY and macrocyclic moieties involved in the electronic coupling in dyads **1–11** (see Figure 1). The theoretical total coupling (V^{Whole} in cm^{-1}) and EET rate constant ($k^{th.}$ in s^{-1}) are also given. We compared both the EET results obtained on the fully-optimised geometry with the Boltzmann averaging following a rotational analysis. The fragmentation scheme and rotated dihedral angles are displayed in Figure S4, the different contributions to the coupling obtained on the fully-optimised geometry are given in Table S6 and the angles, total couplings and relative electronic energy of the rotamers are given in Table S7 in the ESI†.

| Dyad | BODIPY fragment | | Macrocycle fragment | | EET data | | | | | |
| | $\Delta E_{abs}^{th.}$ | f | $\Delta E_{abs}^{th.}$ | f | Optimised geometry | | Boltzmann averaging | | Exp. | |
					V^{Whole}	$k^{th.}$	V^{Whole} ◁	$k^{th.}$	$k^{exp.}$	Ref.
1	2.89	0.652	2.28	0.159	3.4	3.3×10^{9}	2.9	2.4×10^{9}	3.1×10^{10}	17
			2.30	0.030						
2	2.88	0.652	2.28	0.080	5.4	8.4×10^{9}	5.3	7.9×10^{9}	1.2×10^{10}	18
			2.30	0.052						
3l ◇	2.88	0.650	2.31	0.064	2.9	2.4×10^{9}	3.1	2.8×10^{9}	2.2×10^{10}	19
			2.31	0.036						
3f ○	2.85	0.610	2.31	0.057	25.1	1.7×10^{11}	21.6	1.3×10^{11}	2.2×10^{10}	19
			2.31	0.040						
4	2.91	0.627	2.30	0.061	2.9	2.4×10^{9}	4.0	4.7×10^{9}	8.5×10^{9}⋆	20
			2.31	0.037						
5	1.97	0.865	2.31	0.047	39.0	4.3×10^{11}	42.9	5.2×10^{11}	6.6×10^{11}	21
			2.32	0.027						
6-a	2.86	0.564	2.31	0.050	8.2	2.5×10^{10}	10.1	3.9×10^{10}	1.0×10^{12}	22
			2.31	0.046						
6-b	2.86	0.574	2.29	0.064	11.8	5.3×10^{10}	13.7	7.2×10^{10}	1.4×10^{11}	23
			2.29	0.056						
7	2.90	0.625	2.36	0.038	188.9	1.0×10^{13}	186.9	9.9×10^{12}	1.2×10^{11}	24
			2.36	0.004						
8	2.91	0.618	2.31	0.035	17.2	5.4×10^{10}	16.8	5.2×10^{10}	4.5×10^{10}	25
			2.31	0.043						
9	2.89	0.644	2.24	0.065	48.0	3.3×10^{11}	72.1	7.3×10^{11}	2.9×10^{11}	27
			2.25	0.055						
10	2.91	0.622	1.98	0.725	11.7	2.1×10^{9}	25.1	9.6×10^{9}	5.9×10^{10}	68
			2.02	0.622						
11	1.82	1.125	2.43	0.427	19.1	3.6×10^{10}	18.9	3.6×10^{10}	$> 2\times10^{10}$	56
			2.44	0.440						

◇ corresponds to the least stable conformer of **3**

○ correspond to the most stable conformer of **3**

⋆ estimated experimental EET rate constant using the EET efficiency and the lifetime of the donor (details in Section S9 in the ESI†)

◁ corresponds to $\sqrt{p_i(V_i^{Whole})^2/[\sum_i p_i(V_i^{Whole})^2]}$, p_i being the Boltzmann population coefficient for each rotamer i

order of magnitude larger ($k^{th.}=1.8\times10^{12}$ s^{-1}). In this dyad, the EET rate is therefore very sensitive to the details of the computational protocol. Moreover, given the bridge flexibility, a variety of conformations can be expected in solution, between the folded and the linear structures of Figure 5. Each of these conformations would present a different EET rate, possibly faster than the experimental instrument pulse width. [19] In short, a more dynamical description would be required to accurately model the EET in dyad **3**.

For dyad **6-a**, theory is underestimating by two orders of magnitude the EET rate reported in Ref. 22 ($k^{th.}=3.9\times10^{10}$ s^{-1} vs. $k^{exp.}=1.0\times10^{12}$ s^{-1}). We note that additional EET calculations using different fragmentation schemes on the optimised structure have been performed and theory systematically underestimates the experimental rate for that system (with $k^{th.}$ values ranging from 3.0×10^{9} s^{-1} to 2.5×10^{10} s^{-1}, see Section S12 in the ESI†). Surprisingly, the experimental EET rate constant for **6-b** (1.4×10^{11} s^{-1}) is one order of magnitude lower than the one

measured in **6-a**, which has the same core (the only change between the two structures is the substitution pattern on the *meso* phenyl ring of the BODIPY). When comparing the results in both dyads taken in similar conditions (optimisation and EET calculation performed in the same solvent), we obtained a similar coupling value which evidences a limited impact of the substitution on the EET coupling (see Section S12 in the ESI†). This therefore hints that the experimentally reported value for **6-a** is probably coming from the stronger coupling than in **6-b**, consistently with the delocalised nature of the LUMO in **6-a**. In the case of **6-b**, theory provides a good agreement with experiment with a calculated EET rate constant of 7.2×10^{10} s^{-1}. It should be noted that in Ref. 23 the measured dynamics was biexponential, with a contribution of charge separation. Charge-transfer states were excluded in the analysis of Ref. 22, even though the reported EET efficiency (50%) is in contradiction with a picosecond EET rate. Clearly, the dynamics and coupling in molecule **6-a** are more complicated, possibly involving charge-transfer configurations, and cannot be

(a)

$V^{Whole} = 2.9$ cm^{-1}

(b)

$V^{Whole} = 25.1$ cm^{-1}

(c)

$V^{Whole} = 80.1$ cm^{-1}
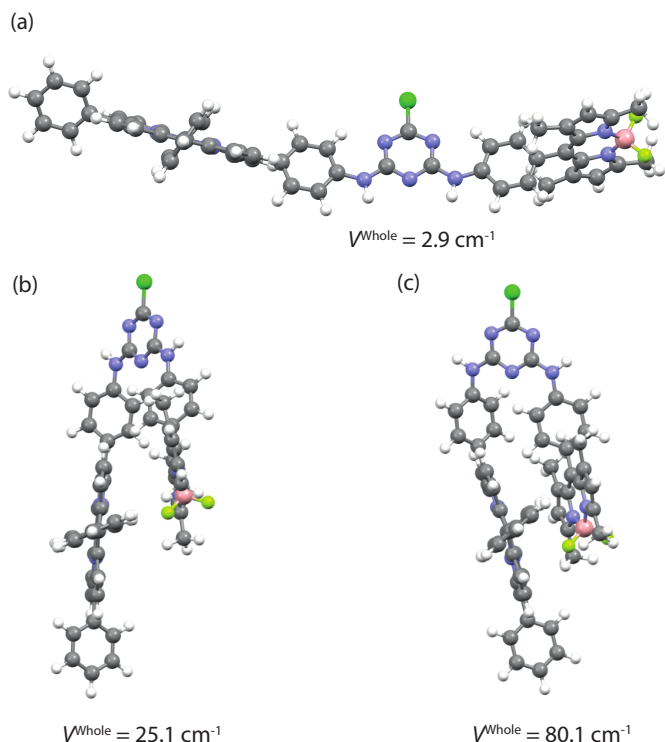
Fig. 5 Structure of the two key conformers of **3**: (a) the "linear" conformation, **3l** determined at the PBE0-D3^{BJ} level; (b) the folded conformation, **3f** optimised at the PBE0-D3^{BJ} level (c) **3f** optimized at the PBE0-D3 level. The total couplings (V^{Whole}) computed on the optimised geometry using the **MC1** fragmentation scheme (see Figure S6 in the ESI†) for the three structures have also been reported.

described as a single EET event. This discrepancy highlights the need of a global analysis of transient spectra, in order to reliably identify the species involved in the excited state dynamics of such dyads.

For dyad **7**, we computed a very large total coupling well above the experimental EET rate constant. This is actually not surprising, given that the computed coupling (almost 200 cm^{-1}) is too large for the assumptions of Eq. (1)[74] and as the orbital analysis showed strong coupling. The large coupling between the two moieties delocalises the excitation, which is reflected in the experimental absorption spectra.[24] In this coupling regime, the excited state dynamics should be described by more complex exciton models.[74]

To conclude, we have shown the strengths and limitations of the present computational approach in reproducing the experimental EET rate constants for the considered dyads. Unsurprisingly, our model fails when the assumptions of Eq. (1) are not valid, e.g., when the electronic coupling is quite strong. Moreover, in very flexible systems, where the dyad can present a variety of conformations, a more extensive sampling would be needed to predict the EET. Acknowledging the limitations of our method, we refrain from the use of flexible bridges for the design of new dyads.

3.3 Design

In this Section, we aim at designing new dyads replacing the macrocyclic moiety by a "pyrrole-free" porphyrin aza-analogue, namely the azacalixphyrin (ACP, see Figure 6a).[72] The ACP presents a strong aromatic character due to the 18 π electrons delocalised over a central 16-membered ring containing four nitrogen atoms (like in porphyrins) while adopting a saddle-like conformation due to the steric repulsion of the internal hydrogen atoms of the phenyl rings. As can be seen in Figure 6b, the macrocycle presents remarkable optical properties with two main absorption bands in the visible and near-infrared regions, i.e., a broad band peaking with a $\lambda_{max} = 890$ nm and an intense band at $\lambda_{max} = 649$ nm.

(a)

(b)
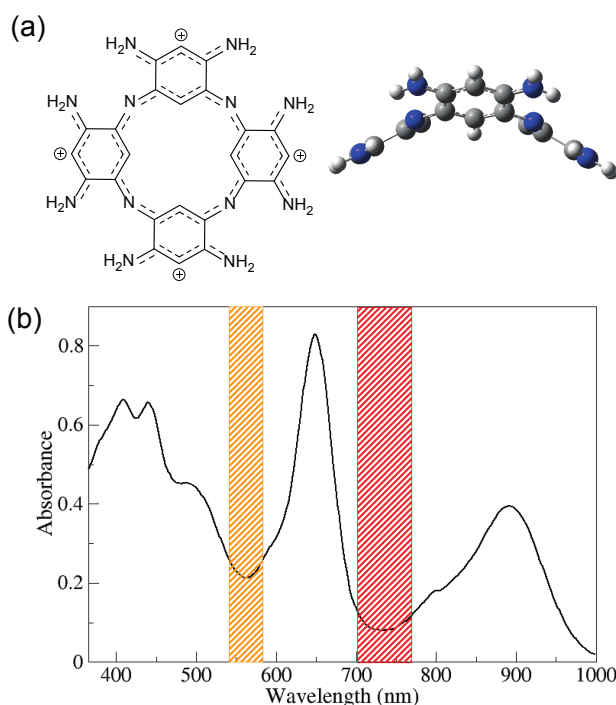
Fig. 6 Representation of the structure of the unsubstituted azacalixphyrin macrocycle (a) and its absorption spectrum in DMSO (b). Adapted with permission from Ref. 72 copyright 2013 Wiley-VCH permission. The orange and red boxes indicates the regions in which the ACP poorly absorbs and hence constitute the two windows in which the donor part, i.e., the BODIPY unit should absorb light.

3.3.1 Choice of the linker and the BODIPY units

As the ACP presents two distinct absorption bands in the visible-NIR domain, we studied energy transfer from different BODIPY units either to the band at ca. 650 nm or to the longest-wavelength band centred at ca. 900 nm. To obtain such energy transfers, one has to design dyads in which the BODIPYs can be excited at wavelengths located respectively in the orange and red zones (see Figure 6b) in which the ACP poorly absorbs. The selected BODIPYs are displayed in Figures 7a and 7b and their spectroscopic signatures, i.e., their measured maximal absorption and fluorescence wavelengths are detailed in Section S17 in the ESI†.
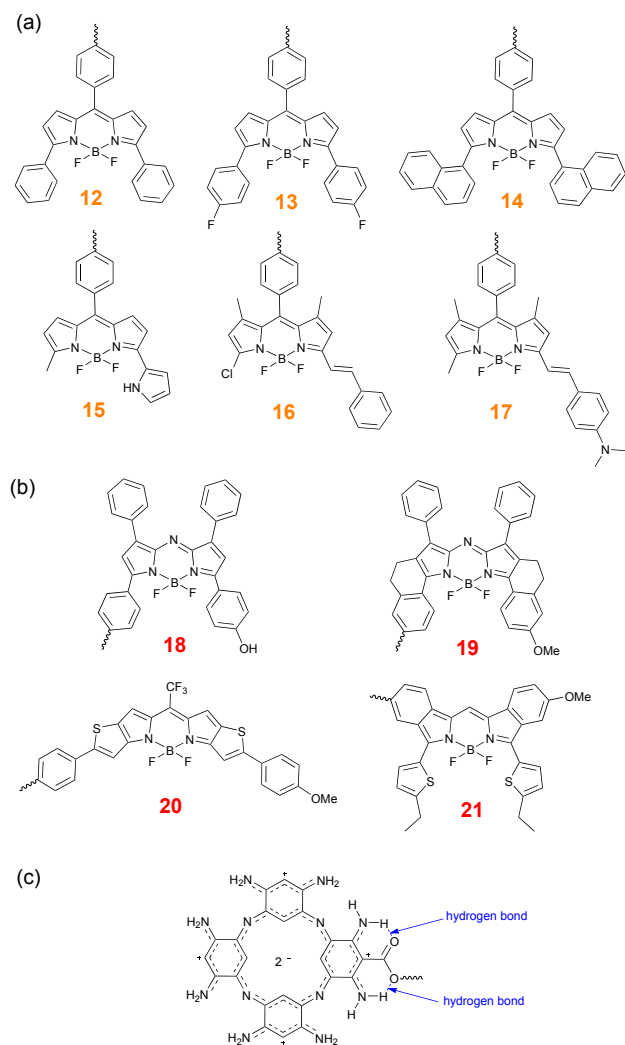
Fig. 7 Representation of the structures of the BODIPYs absorbing in the orange (a) and red (b) regions of the ACP absorption spectrum displayed in Figure 6, and structure of the ACP with the ester linkage (c).

Inspired by the different ZnP-BODIPY systems studied in the previous Section, we selected an ester function as the bridging unit between the macrocycle and the BODIPY (see Figure 7c) similarly to dyad **5** (e.g., see Figure 1). Indeed, this small bridge brings the two units close to each other. Moreover, placing the bridge on a central carbon atom between two external amino groups enables the ester function to interact through hydrogen bonds with these peripheral groups, which locks the relative position of the linker and the macrocycle and limits the conformational freedom. The optimized structure of all dyads indeed shows that the substituted phenyl ring, its amino groups and the ester function are coplanar (see the optimized structure of **12** displayed in Figure S17 in the ESI†) and this statement holds when starting the optimisation from a geometry presenting a perpendicular angle between the ester function and the phenyl ring.

In this configuration, the orientation between the two units seems optimal to reach a large coupling value. To evidence the importance of these hydrogen bonds, we modelled the parent compound of dyad **12** in which all the peripheral amino functions have been replaced with dimethylamino groups, and denoted this structure **12-Me**. The optimized structure of **12-Me** is displayed in Figure S18 in the ESI†. As expected, the steric repulsion brought by the methyl groups induces a large torsion of the ester function, that becomes almost perpendicular to the plane of the substituted phenyl ring of the ACP. A comparison between the EET couplings of **12** and **12-Me** can be found in Section S19 in the ESI† and, as expected, the couplings are larger in the former (ca. 35 cm^{-1}) than in the latter (ca. 13 cm^{-1}), the EET rate constant being almost one order of magnitude larger in **12** ($k^{th.} = 10^{11}$ s^{-1}). However, while the rotation of the bridge with respect to the ACP can be frozen thanks to hydrogen bonds, this does not prevent rotations between the linkage and the BODIPY. We therefore performed a rotational analysis for **12**, the results are reported in Section S20 in the ESI†. The same strategy as for the experimental dyads **1**–**11** have been applied, that is, to optimise all the rotamers while keeping the dihedral angle Φ frozen. Consistently with the **12-Me** case, going from the optimised geometry to a 90° dihedral angle between the bridge and the BODIPY (see Figure S19 in the ESI†) yields a decrease of the EET coupling from 33.2 cm^{-1} to 6.7 cm^{-1}. Averaging the values according to Boltzmann population, we obtain a total coupling that is 23.5 cm^{-1} and a rate constant of 1.6×10^{11}. While the coupling value is 1.4 times lower when accounting for the rotation, the rate constant remains of the same order of magnitude ($\sim 10^{11}$). In the following, we only discuss the EET coupling computed on the fully-optimised structures while keeping in mind that the values have been computed in an "ideal" orientation. If one accounts for the rotational effect, the total coupling values would be slightly lower but the EET rate constant would be the same order of magnitude.

3.3.2 Excitation on the entire dyad 12

To ascertain that there is no electronic communication between the ACP and BODIPY units and to ease the choice of an adequate fragmentation scheme for direct coupling calculations, we computed the excitations of the entire dyad **12**. The transition energies, oscillator strengths and MO composition of the first seven transitions are listed in Table 6 and the MOs are displayed in Figure 8. The MOs involved in the four first excited states are localised on the ACP moiety whereas the MOs involved in S$_7$ are localised on the BODIPY unit, supporting the validity of the weak electronic coupling hypothesis. As in the porphyrinoid systems, the two bands of the ACP are each constituted of two quasi-degenerated excited states. In contrast to dyad **1**, however, the MOs localised on the macrocyclic moiety do not present any density on the linkage while one observes a slight delocalisation of the electronic density on the bridge for the LUMO+2 that is centred on the BODIPY unit. This clearly indicates that the **MC2** fragmentation scheme (see Figure S16 in the ESI†) should be used to model EET in these systems, i.e., the bridge has to be included in the BODIPY fragment rather that in the ACP fragment.

Table 6 Transition energy ($\Delta E_{abs}^{th.}$ in eV), oscillator strength (f) and molecular orbital (MO) composition of the first excited states in **12**.

State	$\Delta E_{abs}^{th.}$	f	MO composition (CI coefficient)
S_1	1.59	0.094	HOMO→LUMO (0.489)
			HOMO-1→LUMO+1 (-0.454)
S_2	1.59	0.062	HOMO→LUMO+1 (0.474)
			HOMO-1→LUMO (0.470)
S_3	2.06	0.465	HOMO-1→LUMO+1 (0.509)
			HOMO→LUMO (0.469)
S_4	2.09	0.415	HOMO-1→LUMO (0.495)
			HOMO→LUMO+1 (0.488)
S_5^a	2.17	0.000	HOMO-2→LUMO (0.705)
S_6^a	2.22	0.000	HOMO-2→LUMO+1 (0.705)
S_7	2.48	0.685	HOMO-2→LUMO+2 (0.705)

^{a} Note that this state corresponds to a spurious (non-physical) charge transfer between the two units
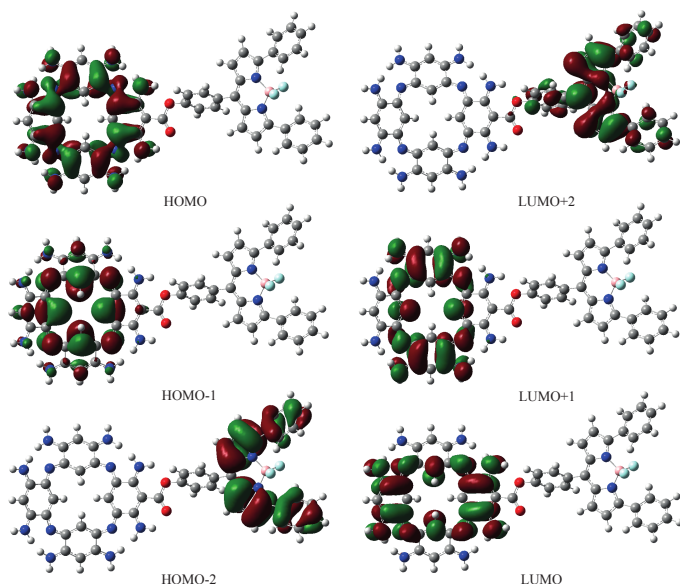
Fig. 8 Molecular orbitals (isovalue = 0.02 a.u.) involved in the first excitations of **12**.

3.3.3 EET results

Let us first analyse the results in dyads **12–17**, in which the energy is transferred from the BODIPY to the ACP band at ca. 650 nm. The couplings obtained for dyads **12–14** are almost the same (ca. 30 cm^{-1}), corresponding to rate constants of ~10^{11} s^{-1} (see Table 7). The couplings increase in dyads **15–17** and attain the very large value of 99.0 cm^{-1} in **17**, the rate constant becoming one order of magnitude larger than in dyads **12–14**.

We note that the BODIPY core is symmetrically substituted in **12–14**, but asymmetrically substituted in **15–17**. In order to confirm that symmetry is the key here, we designed two new dyads, namely **12-asym** and **15-sym** (see Figure S20 in the ESI†) in which the BODIPY unit has been either asymmetrised (we removed one of the two phenyl rings on a pyrrolic unit of BODIPY **12**) or symmetrised (we added the same group on the unsubstituted pyrrolic ring in BODIPY **15**). The results are reported

in Table S21 in the ESI† and consistently with the previous observation, the total coupling in dyads containing an asymmetric BODIPY (61.4 cm^{-1} for **12-asym** and 74.1 cm^{-1} for **15**) is larger than the value obtained in dyads containing a symmetric BODIPY unit (33.2 cm^{-1} for **12** and 34.7 cm^{-1} for **15-sym**). If we examine the magnitude of the transition dipole moment towards the first excited state in the BODIPY (Table S20 in the ESI†), we note that the transition dipole moment is between 3.2 and 3.4 a.u. and remains smaller than in asymmetric units (between 3.6 and 5.0 a.u.). However, it is not the case when comparing **12** to **12-asym** and **15** to **15-sym**. Indeed, in both cases, the transition dipole moments are smaller in the asymmetric structures. We next compared the different contributions to the total coupling (Tables S20 and S21 in the ESI†). For symmetric compounds, i.e., **12–14** and **15-sym**, the major contribution arises from the coupling between the first excited state of the BODIPY (S_1^{BODIPY}) and the third excited state of the ACP (S_3^{ACP}), the S_1^{BODIPY}/S_4^{ACP} coupling being almost negligible (smaller than 10 cm^{-1}). In contrast, in dyads containing asymmetric BODIPYs, i.e., **15–17** and **12-asym**, both S_1^{BODIPY}/S_3^{ACP} and S_1^{BODIPY}/S_4^{ACP} significantly contribute to the total response, the latter being systematically larger. Therefore, the increase of the total coupling in dyad presenting asymmetric BODIPY units is mainly due to a change in the orientation of the transition dipole moment of the BODIPY unit rather than to an increase of its the magnitude. In Figure 9, we display the transition dipole moment of the two units in dyads **12** and **12-asym** (Figure 9a) and in dyads **15** and **15-sym** (Figure 9b). It is clear that, in contrast with dyads in which the BODIPY unit is symmetric, in dyads **12-asym** and **15**, the transition dipole moment of the BODIPY moiety has a component along the axis connecting the two molecules (R_{DA}) which enhances the point-dipole coupling with the ACP transition dipole.

We now consider the energy transfers from a BODIPY unit to the longest-wavelength band of the ACP. We can compare dyads **5** and **18** to evaluate the impact on the coupling when replacing the zinc porphyrin by the ACP macrocycle. To allow a consistent comparison, we re-optimised and computed the EET couplings in dyad **5** using the same solvent (DMSO) as in **18**. The increase in solvent polarity when going from toluene ($\varepsilon = 2.4$) to DMSO ($\varepsilon = 46.8$) induces a variation of the total coupling from 39.0 cm^{-1} to 46.5 cm^{-1} in **5** (see Section S23 in the ESI†). Replacing ZnP with ACP induces an increase of the total coupling from 46.5 cm^{-1} to 64.2 cm^{-1}, but the EET constants remain similar in both dyads as the spectral overlap between the emission of the BODIPY and the absorption of the ACP is smaller than in dyad **5**.

In dyads **19–21** the BODIPY units have been carefully chosen to maximise the spectral overlap (above 1.5 eV^{-1}) with the redmost ACP absorption band. The computed EET coupling is large for all dyads (ca. 80 cm^{-1}) and this holds for the EET rate constant (10^{12} s^{-1}). From the contributions to the total coupling for these dyads (reported in Table S20 in the ESI†), we see that both the S_1^{BODIPY}/S_1^{ACP} and S_1^{BODIPY}/S_2^{ACP} pairs contribute to the total coupling, the larger contribution arising from the former.

To conclude, replacing the porphyrin with the azacalixphyrin allows to increase the coupling in BODIPY–macrocyclic dyads. We showed that the EET rate constant of both energy transfers (BOD-

Table 7 Calculated transition energies ($\Delta E_{abs}^{th.}$ in eV) and oscillator strengths (f) of the excited states of the BODIPY and macrocyclic moieties involved in the electronic coupling of dyads **12–21** represented in Figure 7. The total coupling (V^{Whole} in cm^{-1}), EET rate constant ($k^{th.}$ in s^{-1}) and spectral overlap (J in ev^{-1}) are also given. The different contributions to the coupling can be found in Table S20 the ESI†. The experimental maximal emission wavelength ($\lambda_{em.}^{exp.}$ in nm) of the BODIPY is also given.

band@ 650 nm	BODIPY fragment				ACP fragment		EET data		
	$\Delta E_{abs}^{th.}$	f	$\lambda_{em}^{exp.}$	Ref.	$\Delta E_{abs}^{th.}$	f	J	V^{Whole}	$k^{th.}$
12	2.48	0.697	592	113	2.07	0.395	1.92	33.2	3.1×10^{11}
					2.07	0.392			
13	2.46	0.695	590	114	2.07	0.395	1.84	33.1	2.9×10^{11}
					2.07	0.393			
14	2.31	0.592	607	114	2.07	0.396	2.54	28.9	3.1×10^{11}
					2.07	0.392			
15	2.43	0.779	600	113	2.07	0.395	2.26	74.1	1.8×10^{12}
					2.07	0.393			
16	2.26	0.873	579	114	2.07	0.395	1.36	41.1	3.4×10^{11}
					2.07	0.393			
17	2.07	1.289	660	114	2.07	0.396	2.73	99.0	3.9×10^{12}
					2.07	0.393			
band@ 900 nm	BODIPY				ACP		EET data		
	$\Delta E_{abs}^{th.}$	f	$\lambda_{em}^{exp.}$	Ref.	$\Delta E_{abs}^{th.}$	f	J	V^{Whole}	$k^{th.}$
18	1.99	0.892	715	114	1.58	0.062	0.57	64.2	3.5×10^{11}
					1.58	0.066			
19	1.90	0.957	751	113	1.58	0.062	1.27	78.8	1.2×10^{12}
					1.59	0.067			
20	1.93	1.715	754	113	1.58	0.062	1.34	84.7	1.4×10^{12}
					1.59	0.067			
21	1.86	0.798	780	113	1.58	0.062	1.99	81.0	1.90×10^{12}
					1.59	0.066			

(a)

(b)
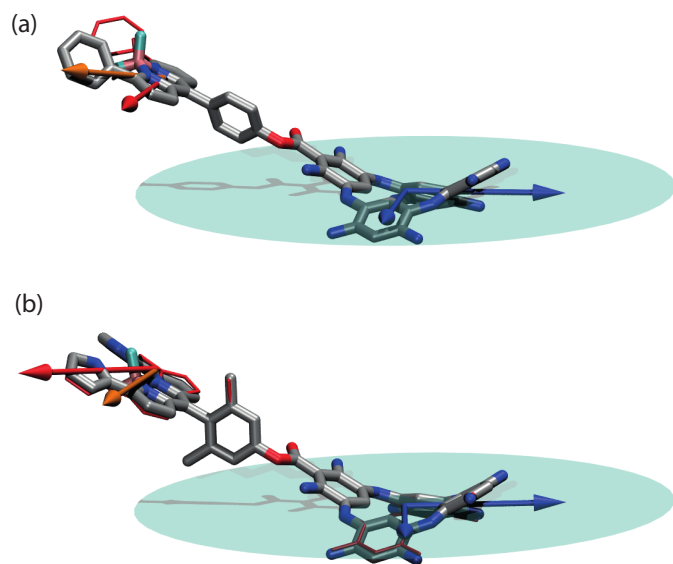
Fig. 9 Representation of the transition dipole moments of the BODIPY and ACP units (a) in dyads **12** and its asymmetric counterpart, **12-asym**, and (b) in dyads **15** and its symmetric analogue, **15-sym**. The red representations and dipoles correspond to the unmodified structure **12** and **15** whereas the element-coloured representation and orange dipole refer to **12-asym** and **15-sym** dyads. The transition dipole moments of the ACP and the plane of the dipole are represented in blue.

IPY to the two bands of the ACP) can reach 10^{12} s^{-1}, highlighting the potential of ACP macrocycles beyond their current applica-

tions.

4 Conclusions

We have investigated the singlet-singlet excitation energy transfer in more than twenty BODIPY-macrocycle molecular dyads. We first aimed at accurately modelling the EET in known systems for which the rate constant have been measured experimentally, so to design on solid grounds new assemblies incorporating an azacalixphyrin macrocycle and presenting improved EET properties. To reach these goals, we used a theoretical model combining TD-DFT for obtaining transition densities and the PCM implicit solvation model to account for solvent effects.

In a first step, we have applied several strategies to compute EET in a representative BODIPY-zinc porphyrin dyad in order to select an appropriate computational protocol. Among the two different methods that were used to calculate EET, i.e., FED and direct coupling that starts from the excitations computing on the full system or for the separated donor and acceptor fragments, respectively, we have shown that: (i) in the FED method, the convergence of the total coupling value is only reached when using a multi-state FED approach, including several excited states in the calculation of the coupling; (ii) both multi-state FED and direct coupling provide very similar coupling values, indicating that a through-space rather than a through-bond energy transfer occurs and that the computationally cheaper direct coupling method can be safely applied in these dyads. Within this approach, we have studied the impact of the definition of the fragments on the total coupling and we have deduced that the following frag-

mentation scheme is adequate: (i) the BODIPY part including its *meso* phenyl ring; and (ii) the macrocyclic fragment encompassing the tetraphenyl zinc porphyrin and the ethynyl bridge. This definition has been supported by the analysis of the molecular orbitals involved in the first dipole-allowed excitations of the full system. We have also assessed the description of the transition density of both fragments, varying the underlying DFT parameters (exchange-correlation functional and basis set), and we validated the use of PBE0 in combination with the compact 6-31+G(d) atomic basis set. The impact of the rotation and the orientation of the phenyl rings of the porphyrin have also been evaluated.

Next, we have assessed the robustness of our computational protocol by comparing the theoretical and experimental EET rate constants in twelve BODIPY-porphyrinoid assemblies presenting various donor, acceptor and linker moieties so to be representative of the diversity of these dyads. In most cases, theory is able to reproduce the order of magnitude of the experimentally determined rate constants. However, we found some important limitations of the used protocol, mainly related to the applicability of Eq. (1) and to the conformational sampling in flexible dyads. Is it important to highlight that these shortcomings are intrinsic to the simplified EET theory and protocol used here, and not to the quantum chemical calculation of the relevant electronic couplings, which are robust with respect to level of theory and basis set.

Finally, we have designed ten new molecular entities, in which a BODIPY fluorophore is coupled to an azacalixphyrin macrocycle. We have investigated the electronic energy transfer from the BODIPY to the ACP, considering EET to the two distinct absorption bands of the ACP, localised in the visible and near-IR regions of the spectrum. We have shown that replacing the porphyrin by the azacalixphyrin allows to increase the electronic coupling and we have shown that the symmetry of the BODIPY unit also plays a crucial role in the EET coupling. Indeed, it turns out that the coupling is larger with asymmetrically-substituted BODIPYs than with symmetrically-substituted dyes, a fact that can be attributed to a more favourable orientation of the transition dipole moment in the former compounds. These new molecular dyads, comprising an azacalixphyrin, display enhanced EET rate constants that can reach 10^{12} s^{-1} and therefore highlight the interest of ACPs as building blocks in molecular light-harvesting antennas.

5   Acknowledgments

References

1 K. M. Kadish, K. M. Smith and R. Guilard, *Handbook of Porphyrin Science: With Applications to Chemistry, Physics, Materials Science, Engineering, Biology and Medicine*, World Scientific, 2010.

2 M. Senge, M. Fazekas, E. Notaras, W. Blau, M. Zawadzka, O. Locos and E. Ni Mhuircheartaigh, *Adv. Mater.*, 2007, **19**, 2737–2774.

3 M. Calvete, G. Y. Yang and M. Hanack, *Synth. Met.*, 2004, **141**, 231–243.

4 Y. Ding, W.-H. Zhu and Y. Xie, *Chem. Rev.*, 2017, **117**, 2203–2256.

5 R. Paolesse, S. Nardis, D. Monti, M. Stefanelli and C. Di Natale, *Chem. Rev.*, 2017, **117**, 2517–2583.

6 M. Ethirajan, Y. Chen, P. Joshi and R. K. Pandey, *Chem. Soc. Rev.*, 2011, **40**, 340–362.

7 R. Bonnett, *Chem. Soc. Rev.*, 1995, **24**, 19–33.

8 L.-L. Li and E. W.-G. Diau, *Chem. Soc. Rev.*, 2013, **42**, 291–304.

9 M. V. Martinez-Diaz, G. de la Torre and T. Torres, *Chem. Commun.*, 2010, **46**, 7090–7108.

10 A. Loudet and K. Burgess, *Chem. Rev.*, 2007, **107**, 4891–4932.

11 D. Frath, J. Massue, G. Ulrich and R. Ziessel, *Angew. Chem. Int. Ed.*, 2014, **53**, 2290–2310.

12 G. Ulrich, R. Ziessel and A. Harriman, *Angew. Chem. Int. Ed.*, 2008, **47**, 1184–1201.

13 A. B. Nepomnyashchii and A. J. Bard, *Acc. Chem. Res.*, 2012, **45**, 1844–1853.

14 T. K. Khan, M. Bröring, S. Mathur and M. Ravikanth, *Coord. Chem. Rev.*, 2013, **257**, 2348–2387.

15 K. Ladomenou, V. Nikolaou, G. Charalambidis, A. Charisiadis and A. G. Coutsolelos, *C. R. Chim.*, 2017, **20**, 314–322.

16 A. Bessette and G. S. Hanan, *Chem. Soc. Rev.*, 2014, **43**, 3342–3405.

17 C. Lee, J. Jang, C. Kim, J. Jung, B. Park, J. Park, W. Choi, Y.-K. Han, T. Joo and J. Park, *Chem. Eur. J.*, 2010, **16**, 5586–5599.

18 E. Maligaspe, T. Kumpulainen, N. K. Subbaiyan, M. E. Zandler, H. Lemmetyinen, N. V. Tkachenko and F. D'Souza, *Phys. Chem. Chem. Phys.*, 2010, **12**, 7434–7444.

19 T. Lazarides, G. Charalambidis, A. Vuillamy, M. Réglier, E. Klontzas, G. Froudakis, S. Kuhri, D. M. Guldi and A. G. Coutsolelos, *Inorg. Chem.*, 2011, **50**, 8926–8936.

20 M. J. Leonardi, M. R. Topka and P. H. Dinolfo, *Inorg. Chem.*, 2012, **51**, 13114–13122.

21 F. D'Souza, A. N. Amin, M. E. El-Khouly, N. K. Subbaiyan, M. E. Zandler and S. Fukuzumi, *J. Am. Chem. Soc.*, 2012, **134**, 654–664.

22 M. E. El-Khouly, C. A. Wijesinghe, V. N. Nesterov, M. E. Zandler, S. Fukuzumi and F. D'Souza, *Chem. Eur. J.*, 2012, **18**, 13844–13853.

23 F. D'Souza, C. A. Wijesinghe, M. E. El-Khouly, J. Hudson, M. Niemi, H. Lemmetyinen, N. V. Tkachenko, M. E. Zandler and S. Fukuzumi, *Phys. Chem. Chem. Phys.*, 2011, **13**, 18168–18178.

24 Q.-Q. Hu, Y.-Z. Zhu, S.-C. Zhang, Y.-Z. Tong and J.-Y. Zheng,

Dalton Trans., 2015, **44**, 15523–15530.

25 H.-J. Xu, A. Bonnot, P.-L. Karsenti, A. Langlois, M. Abdel-hameed, J.-M. Barbe, C. P. Gros and P. D. Harvey, *Dalton Trans.*, 2014, **43**, 8219–8229.

26 N. T. Nguyen, B. Verbelen, V. Leen, E. Waelkens, W. Dehaen and M. Kruk, *J. Lumin.*, 2016, **179**, 306–313.

27 T. Lazarides, S. Kuhri, G. Charalambidis, M. K. Panda, D. M. Guldi and A. G. Coutsolelos, *Inorg. Chem.*, 2012, **51**, 4193–4204.

28 D. Gao, S. M. Aly, P.-L. Karsenti, G. Brisard and P. D. Harvey, *Dalton Trans.*, 2017, **46**, 6278–6290.

29 F. Li, S. I. Yang, Y. Ciringh, J. Seth, C. H. Martin, D. L. Singh, D. Kim, R. R. Birge, D. F. Bocian, D. Holten and J. S. Lindsey, *J. Am. Chem. Soc.*, 1998, **120**, 10001–10017.

30 C. Y. Lee and J. T. Hupp, *Langmuir*, 2010, **26**, 3760–3765.

31 J. Warnan, F. Buchet, Y. Pellegrin, E. Blart and F. Odobel, *Org. Lett.*, 2011, **13**, 3944–3947.

32 D. Kumaresan, N. Agarwal and M. Ravikanth, *J. Chem. Soc., Perkin Trans. 1*, 2001, 1644–1648.

33 M. D. Weber, V. Nikolaou, J. E. Wittmann, A. Nikolaou, P. A. Angaridis, G. Charalambidis, C. Stangel, A. Kahnt, A. G. Coutsolelos and R. D. Costa, *Chem. Commun.*, 2016, **52**, 1602–1605.

34 F. D'Souza, P. M. Smith, M. E. Zandler, A. L. McCarty, M. Itou, Y. Araki and O. Ito, *J. Am. Chem. Soc.*, 2004, **126**, 7898–7907.

35 B. Brizet, A. Eggenspiller, C. P. Gros, J.-M. Barbe, C. Goze, F. Denat and P. D. Harvey, *J. Org. Chem.*, 2012, **77**, 3646–3650.

36 N. T. Nguyen, B. Verbelen, V. Leen, E. Waelkens, W. Dehaen and M. Kruk, *J. Lumin.*, 2016, **179**, 306–313.

37 A. Eggenspiller, A. Takai, M. E. El-Khouly, K. Ohkubo, C. P. Gros, C. Bernhard, C. Goze, F. Denat, J.-M. Barbe and S. Fukuzumi, *J. Phys. Chem. A*, 2012, **116**, 3889–3898.

38 Y. Chen, L. Wan, X. Yu, W. Li, Y. Bian and J. Jiang, *Org. Lett.*, 2011, **13**, 5774–5777.

39 J.-Y. Liu, E. A. Ermilov, B. Röder and D. K. Ng, *J. Porph. Phthalo.*, 2013, **17**, 831–835.

40 K. Ladomenou, T. Lazarides, M. K. Panda, G. Charalambidis, D. Daphnomili and A. G. Coutsolelos, *Inorg. Chem.*, 2012, **51**, 10548–10556.

41 Y. Terazono, G. Kodis, P. A. Liddell, V. Garg, T. A. Moore, A. L. Moore and D. Gust, *J. Phys. Chem. B*, 2009, **113**, 7147–7155.

42 T. K. Khan and M. Ravikanth, *Tetrahedron*, 2011, **67**, 5816–5824.

43 M. Koepf, A. Trabolsi, M. Elhabiri, J. A. Wytko, D. Paul, A. M. Albrecht-Gary and J. Weiss, *Org. Lett.*, 2005, **7**, 1279–1282.

44 S. Pascal, L. Bucher, N. Desbois, C. Bucher, C. Andraud and C. P. Gros, *Chem. Eur. J.*, 2016, **22**, 4971–4979.

45 M. T. Whited, P. I. Djurovich, S. T. Roberts, A. C. Durrell, C. W. Schlenker, S. E. Bradforth and M. E. Thompson, *J. Am. Chem. Soc.*, 2011, **133**, 88–96.

46 W.-J. Shi, R. Menting, E. A. Ermilov, P.-C. Lo, B. Roder and D. K. P. Ng, *Chem. Commun.*, 2013, **49**, 5277–5279.

47 T. Shiragami, K. Tanaka, Y. Andou, S. ichiro Tsunami, J. Matsumoto, H. Luo, Y. Araki, O. Ito, H. Inoue and M. Yasuda, *J. Photochem. Photobiol. A: Chem.*, 2005, **170**, 287–297.

48 C. Göl, M. Malkoç, S. Yeşilot and M. Durmuş, *Dyes Pigm.*, 2014, **111**, 81–90.

49 Y. Rio, W. Seitz, A. Gouloumis, P. Vázquez, J. Sessler, D. Guldi and T. Torres, *Chem. Eur. J.*, 2010, **16**, 1929–1940.

50 J.-Y. Liu, E. A. Ermilov, B. Roder and D. K. P. Ng, *Chem. Commun.*, 2009, 1517–1519.

51 E. A. Ermilov, J.-Y. Liu, D. K. P. Ng and B. Roder, *Phys. Chem. Chem. Phys.*, 2009, **11**, 6430–6440.

52 E. A. Ermilov, J.-Y. Liu, R. Menting, Y.-S. Huang, B. Roder and D. K. P. Ng, *Phys. Chem. Chem. Phys.*, 2016, **18**, 10964–10975.

53 V. Engelhardt, S. Kuhri, J. Fleischhauer, M. Garcia-Iglesias, D. Gonzalez-Rodriguez, G. Bottari, T. Torres, D. M. Guldi and R. Faust, *Chem. Sci.*, 2013, **4**, 3888–3893.

54 S. Osati, H. Ali and J. E. van Lier, *Tetrahedron Lett.*, 2015, **56**, 2049–2053.

55 S. Kuhri, V. Engelhardt, R. Faust and D. M. Guldi, *Chem. Sci.*, 2014, **5**, 2580–2588.

56 R. Ziessel, G. Ulrich, K. Elliott and A. Harriman, *Chem. Eur. J.*, 2009, **15**, 4980–4984.

57 J.-Y. Liu, H.-S. Yeung, W. Xu, X. Li and D. K. P. Ng, *Org. Lett.*, 2008, **10**, 5421–5424.

58 S. Çetindere, B. Çoşut, S. Yeşilot, M. Durmuş and A. Kiliç, *Dyes Pigm.*, 2014, **101**, 234–239.

59 E. T. Eçik, E. Özcan, H. Kandemir, I. F. Sengul and B. Çoşut, *Dyes Pigm.*, 2017, **136**, 441–449.

60 H. B. Gobeze, V. Bandi and F. D'Souza, *Phys. Chem. Chem. Phys.*, 2014, **16**, 18720–18728.

61 L. Giribabu, K. Jain, K. Sudhakar, N. Duvva and R. Chitta, *J. Lumin.*, 2016, **177**, 209–218.

62 Y. Yan, F. Wu, J. Qin, H. Xu, M. Shi, J. Zhou, J. Mack, G. Fomo, T. Nyokong and Z. Shen, *RSC Adv.*, 2016, **6**, 72852–72858.

63 B. Brizet, N. Desbois, A. Bonnot, A. Langlois, A. Dubois, J.-M. Barbe, C. P. Gros, C. Goze, F. Denat and P. D. Harvey, *Inorg. Chem.*, 2014, **53**, 3392–3403.

64 A. Meares, A. Satraitis, N. Santhanam, Z. Yu and M. Ptaszek, *J. Org. Chem.*, 2015, **80**, 3858–3869.

65 K. Yumiko, S. Yutaka and T. Hitoshi, *Chem. Lett.*, 2010, **39**, 953–955.

66 A. Meares, A. Satraitis, J. Akhigbe, N. Santhanam, S. Swaminathan, M. Ehudin and M. Ptaszek, *J. Org. Chem.*, 2017, **82**, 6054–6070.

67 J.-Y. Shin, K. Kim, J. M. Lim, T. Tanaka, D. Kim, K. Kim, H. Shinokubo and A. Osuka, *Chem. Eur. J.*, 2014, **20**, 4574–4582.

68 M. E. El-Khouly, C. Göl, M. M. El-Hendawy, S. Yeşilot and M. Durmuş, *J. Porph. Phthalo.*, 2015, **19**, 261–269.

69 J. Tomasi, B. Mennucci and R. Cammi, *Chem. Rev.*, 2005, **105**, 2999–3094.

70 C.-P. Hsu, Z.-Q. You and H.-C. Chen, *J. Phys. Chem. C*, 2008, **112**, 1204–1212.

71 Z.-Q. You and C.-P. Hsu, *Int. J. Quantum Chem.*, 2014, **114**, 102–115.

72 Z. Chen, M. Giorgi, D. Jacquemin, M. Elhabiri and O. Siri, *Angew. Chem.*, 2013, **125**, 6370–6374.

73 Z. Chen, R. Haddoub, J. Mahé, G. Marchand, D. Jacquemin, J. Andeme Edzang, G. Canard, D. Ferry, O. Grauby, A. Ranguis and O. Siri, *Chem. Eur. J.*, 2016, **22**, 17820–17832.

74 V. May and O. Kühn, in *Excitation Energy Transfer*, Wiley-VCH Verlag GmbH and Co. KGaA, 2011, pp. 467–558.

75 G. D. Scholes, *Annu. Rev. Phys. Chem.*, 2003, **54**, 57–87.

76 Z.-Q. You and C.-P. Hsu, *J. Phys. Chem. A*, 2011, **115**, 4092–

4100.

77 M. F. Iozzi, B. Mennucci, J. Tomasi and R. Cammi, *J. Chem. Phys.*, 2004, **120**, 7029–7040.

78 D. L. Dexter, *J. Chem. Phys.*, 1953, **21**, 836–850.

79 B. P. Krueger, G. D. Scholes and G. R. Fleming, *J. Phys. Chem. B*, 1998, **102**, 5378–5386.

80 G. D. Scholes, *Annu. Rev. Phys. Chem.*, 2003, **54**, 57–87.

81 G. D. Scholes and G. R. Fleming, in *Energy Transfer and Photosynthetic Light Harvesting*, John Wiley and Sons, Inc., 2005, pp. 57–129.

82 C.-H. Yang and C.-P. Hsu, *J. Chem. Phys.*, 2013, **139**, 154104.

83 M. J. Frisch, G. W. Trucks, H. B. Schlegel, G. E. Scuseria, M. A. Robb, J. R. Cheeseman, G. Scalmani, V. Barone, B. Mennucci, G. A. Petersson, H. Nakatsuji, M. Caricato, X. Li, H. P. Hratchian, A. F. Izmaylov, J. Bloino, G. Zheng, J. L. Sonnenberg, M. Hada, M. Ehara, K. Toyota, R. Fukuda, J. Hasegawa, M. Ishida, T. Nakajima, Y. Honda, O. Kitao, H. Nakai, T. Vreven, J. A. Montgomery, Jr., J. E. Peralta, F. Ogliaro, M. Bearpark, J. J. Heyd, E. Brothers, K. N. Kudin, V. N. Staroverov, R. Kobayashi, J. Normand, K. Raghavachari, A. Rendell, J. C. Burant, S. S. Iyengar, J. Tomasi, M. Cossi, N. Rega, J. M. Millam, M. Klene, J. E. Knox, J. B. Cross, V. Bakken, C. Adamo, J. Jaramillo, R. Gomperts, R. E. Stratmann, O. Yazyev, A. J. Austin, R. Cammi, C. Pomelli, J. W. Ochterski, R. L. Martin, K. Morokuma, V. G. Zakrzewski, G. A. Voth, P. Salvador, J. J. Dannenberg, S. Dapprich, A. D. Daniels, Ö. Farkas, J. B. Foresman, J. V. Ortiz, J. Cioslowski and D. J. Fox, *Gaussian 09 Revision D.01*, Gaussian Inc. Wallingford CT, 2009.

84 C. Adamo and V. Barone, *J. Chem. Phys.*, 1999, **110**, 6158–6170.

85 S. Grimme, S. Ehrlich and L. Goerigk, *J. Comput. Chem.*, 2011, **32**, 1456–1465.

86 P. J. Hay and W. R. Wadt, *J. Chem. Phys.*, 1985, **82**, 270–283.

87 W. R. Wadt and P. J. Hay, *J. Chem. Phys.*, 1985, **82**, 284–298.

88 P. J. Hay and W. R. Wadt, *J. Chem. Phys.*, 1985, **82**, 299–310.

89 S. Grimme, J. Antony, S. Ehrlich and H. Krieg, *J. Chem. Phys.*, 2010, **132**, 154104.

90 J. P. Perdew, K. Burke and M. Ernzerhof, *Phys. Rev. Lett.*, 1996, **77**, 3865–3868.

91 J. P. Perdew, K. Burke and M. Ernzerhof, *Phys. Rev. Lett.*, 1997, **78**, 1396–1396.

92 Y. Zhao and D. G. Truhlar, *J. Chem. Phys.*, 2006, **125**, 194101.

93 A. D. Becke, *J. Chem. Phys.*, 1993, **98**, 5648–5652.

94 Y. Zhao and D. G. Truhlar, *Theor. Chem. Acc.*, 2008, **120**,

215–241.

95 T. Yanai, D. P. Tew and N. C. Handy, *Chem. Phys. Lett.*, 2004, **393**, 51–57.

96 O. A. Vydrov and G. E. Scuseria, *J. Chem. Phys.*, 2006, **125**, 234109.

97 S. Caprasecca, C. Curutchet and B. Mennucci, *J. Chem. Theory Comput.*, 2012, **8**, 4462–4473.

98 C. Azarias, R. Russo, L. Cupellini, B. Mennucci and D. Jacquemin, *Phys. Chem. Chem. Phys.*, 2017, **19**, 6443–6453.

99 C. Curutchet, A. Munoz-Losa, S. Monti, J. Kongsted, G. D. Scholes and B. Mennucci, *J. Chem. Theory Comput.*, 2009, **5**, 1838–1848.

100 J. Wang, P. Cieplak, J. Li, T. Hou, R. Luo and Y. Duan, *J. Phys. Chem. B*, 2011, **115**, 3091–3099.

101 S. Caprasecca, C. Curutchet and S. Jurinovich, *PolChat: A polarisation-consistent charge fitting tool, 2014*, Department of Chemistry, University of Pisa, Italy.

102 P.-O. Löwdin, *Advances in Quantum Chemistry*, Academic Press, 1970, vol. 5, pp. 185–199.

103 R. Cammi and B. Mennucci, *J. Chem. Phys.*, 1999, **110**, 9877–9886.

104 C. Wiebeler, F. Plasser, G. J. Hedley, A. Ruseckas, I. D. W. Samuel and S. Schumacher, *J. Phys. Chem. Lett.*, 2017, **8**, 1086–1092.

105 D. J. Tozer, *J. Chem. Phys.*, 2003, **119**, 12697–12699.

106 A. Dreuw and M. Head-Gordon, *J. Am. Chem. Soc.*, 2004, **126**, 4007–4016.

107 V. N. Nemykin, R. G. Hadt, R. V. Belosludov, H. Mizuseki and Y. Kawazoe, *J. Phys. Chem. A*, 2007, **111**, 12901–12913.

108 R. Improta, C. Ferrante, R. Bozio and V. Barone, *Phys. Chem. Chem. Phys.*, 2009, **11**, 4664–4673.

109 L. Petit, A. Quartarolo, C. Adamo and N. Russo, *J. Phys. Chem. B*, 2006, **110**, 2398–2404.

110 A. D. Quartarolo, N. Russo, E. Sicilia and C. Adamo, in *The Contribution of Theoretical Chemistry to the Drug Design in Photodynamic Therapy*, ed. T. Nyokong and V. Ahsen, Springer Netherlands, Dordrecht, 2012, pp. 121–134.

111 B. Le Guennic and D. Jacquemin, *Acc. Chem. Res.*, 2015, **48**, 530–537.

112 Y. A. Berlin, F. C. Grozema, L. D. A. Siebbeles and M. A. Ratner, *J. Phys. Chem. C*, 2008, **112**, 10988–11000.

113 Y. Ni and J. Wu, *Org. Biomol. Chem.*, 2014, **12**, 3774–3791.

114 A. Loudet and K. Burgess, *Chem. Rev.*, 2007, **107**, 4891–4932.

Graphical Abstract

EET